

## JGR Solid Earth

## RESEARCH ARTICLE

10.1029/2019JB017929

## Key Points:

- The autocorrelation of teleseismic  $P$ -waves and their coda can recover the layered structure of the crust
- We add a term to  $H$ - $\kappa$  stacking that considers the Moho-reflected  $P$ -wave to constrain average  $P$ -wave velocity in the crust
- The consideration of uncertainties in  $P$ -wave velocity estimates leads to more accurate estimations of correlated uncertainties in crustal properties

## Supporting Information:

- Supporting Information S1
- Movie S1
- Table S1

## Correspondence to:

J. R. Delph,  
jdelph@uoregon.edu

## Citation:

Delph, J. R., Levander, A., & Niu, F. (2019). Constraining crustal properties using receiver functions and the autocorrelation of earthquake-generated body waves. *Journal of Geophysical Research: Solid Earth*, 124. <https://doi.org/10.1029/2019JB017929>

Received 26 APR 2019

Accepted 2 AUG 2019

Accepted article online 7 AUG 2019

# Constraining Crustal Properties Using Receiver Functions and the Autocorrelation of Earthquake-Generated Body Waves

Jonathan R. Delph<sup>1,2</sup> , Alan Levander<sup>1</sup> , and Fenglin Niu<sup>1</sup> 

<sup>1</sup>Department of Earth, Environmental, and Planetary Sciences, Rice University, Houston, TX, USA, <sup>2</sup>Now at Department of Earth Sciences, University of Oregon, Eugene, OR, USA

**Abstract** Passive seismic methods for imaging the discontinuity structure of Earth have primarily focused on differences in vertically and radially polarized energy in the coda of earthquake-generated body waves (e.g., receiver functions). To convert the timing of scattered wave arrivals to depth, three parameters must be known or inferred: depth or layer thickness ( $H$ ),  $P$ -wave velocity ( $V_P$ ), and  $S$ -wave velocity ( $V_S$ ). A common way to solve for these parameters is through  $H$ - $\kappa$  stacking analysis, in which layer thickness and the ratio between  $V_P$  and  $V_S$  ( $\kappa$ ) is calculated while holding one of the velocity parameters constant. However, this assumption biases estimates of layer properties and leads to uncertainties that are not appropriately quantified. As these results are commonly used as starting models for more complex seismic or geodynamic analyses, these assumptions can propagate much further than the initial study. In this study, we introduce independent observations from body-wave autocorrelations that can help constrain this underdetermined problem.  $P$ -wave autocorrelation allows for the recovery of the Moho-reflected  $P$ -wave phase from teleseismic earthquakes, which is removed during deconvolution in the calculation of receiver functions. As the Moho-reflected  $P$ -wave is independent of  $V_S$ , this constraint allows us to create a system of equations that better quantifies the thickness,  $V_P$ , and  $V_S$  of a layer and produces a more appropriate estimation of associated uncertainties. We apply this to 88 seismic stations that are spatially distributed throughout the United States to obtain a model of crustal variability that is unbiased by a priori assumptions of velocity structure.

## 1. Introduction

The vast increase in publicly available seismic data has led to innovative analyses that exploit coherent, low signal-to-noise ratio arrivals through the cross correlation of seismic waves. Generally, this involves comparing and stacking records from contemporaneously operating stations to obtain the Green's function between the stations. These interferometry methods are commonly used for measuring surface wave velocities (e.g., Lin et al., 2008; Shapiro et al., 2005) and show promise for elucidating discontinuity structure using body waves (Draganov et al., 2009; Lin et al., 2013; Poli, Campillo, et al., 2012; Poli, Pedersen, et al., 2012). More recently, attempts to estimate Earth's discontinuity structure through the cross correlation of seismic signals at individual stations, or autocorrelation, have had varied degrees of success (Gorbatov et al., 2013; Heath et al., 2018; Kennett, 2015; Kennett et al., 2015; Oren & Nowack, 2017; Sun & Kennett, 2017; Tibuleac & von Seggern, 2012). Though it has been theoretically proven that the autocorrelation of an ongoing wave at a station is equivalent to the reflectivity response of the underlying media (Claerbout, 1968; Frasier, 1970; Gorbatov et al., 2013), most studies prefer to estimate discontinuity structure by deconvolving different seismic components during the coda of direct arrivals from earthquakes to highlight body-wave conversions (e.g., receiver functions; Langston, 1979).

Recent improvements in data processing, however, have renewed interest in using seismic autocorrelation to estimate the discontinuity structure beneath a station (Oren & Nowack, 2017; Phạm & Tkalčić, 2017), resulting in convincing results especially when a coherent seismic source (such as an earthquake) is analyzed (Kim et al., 2019; Phạm & Tkalčić, 2017). By autocorrelating the direct  $P$ -wave with its coda, not only are phases associated with  $P$ -to- $S$ -wave conversions observed, as in receiver functions, but the backscattered/reflected  $P$ -wave is also recovered, a phase that cancels during deconvolution in the receiver function calculation (Figure 1). An inherent mathematical characteristic of the autocorrelation procedure is

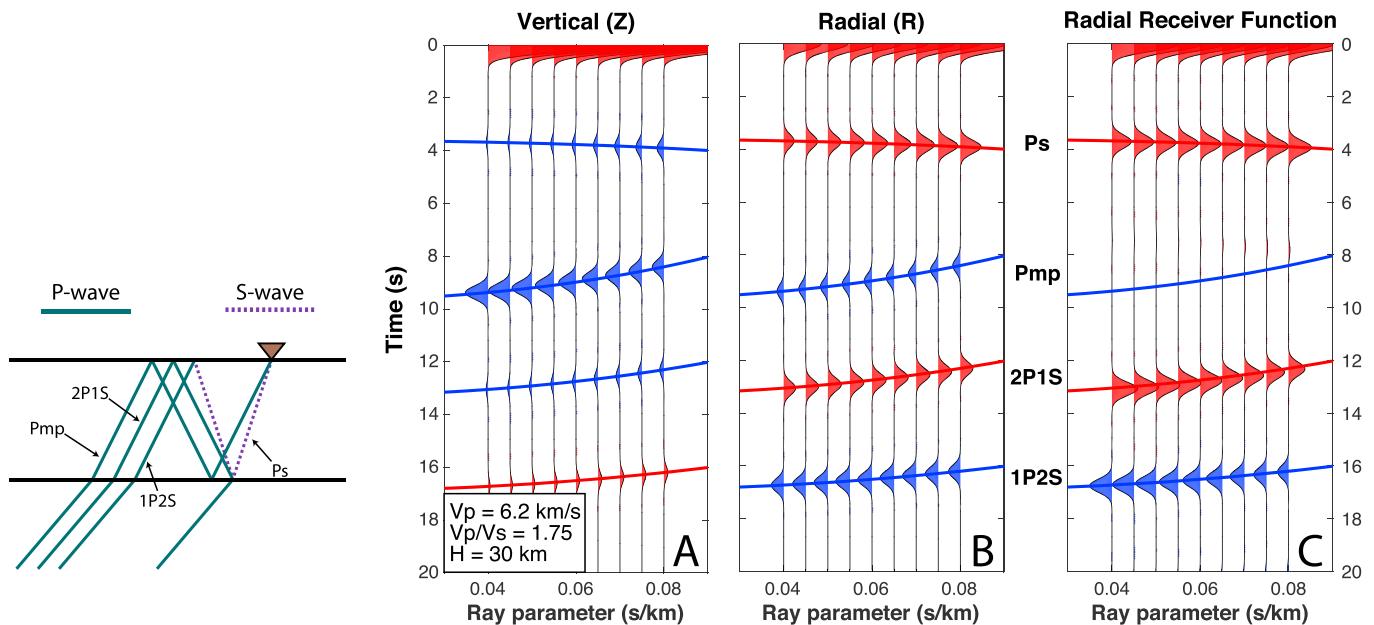


**Figure 1.** (Far left) Schematic representation of a plane wave impinging on a layer to produce the synthetic vertical (A) and radial (B) component seismograms and receiver functions (C). The layer consists of a thickness of 30 km with a  $V_P = 6.2$  km/s and  $V_P/V_S$  ratio of 1.75. A range of different ray parameters are modeled to illustrate moveout for the different phases at teleseismic distances (30–95 epicentral degrees). Lines connecting peaks are colored by expected polarity for that phase (blue = negative and red = positive). Receiver functions highlight phases with opposite polarities best, while the Pmp phase is not apparent.

that it turns arbitrarily shaped primary signals into simple pulse-like arrivals that correspond to the Green's function of the structure it samples. When applied to earthquake-generated signals, this turns the source-time function into a simple pulse that highlights velocity discontinuities, as reflected/transmitted wavelets across an impedance contrast are simply scaled versions of the input wavelet. The final product is a signal with a similar character to that of receiver functions. In this study, we first show the feasibility of obtaining the discontinuity structure of the Earth using autocorrelations of the vertical and radial component seismograms from both synthetic and real teleseismic events. We then combine these results with receiver functions through a modified  $H$ - $\kappa$  stacking analysis approach (Zhu & Kanamori, 2000) to obtain information about the layered structure of the Earth beneath a station. By introducing autocorrelations, we obtain an arrival that independently constrains the average  $P$ -wave velocity structure of a layer, a parameter commonly assumed in  $H$ - $\kappa$  stacking analysis. This approach also allows for a more appropriate estimation of correlated uncertainties between crustal properties (e.g.,  $V_P$ ,  $V_S$ , and layer thickness), which can be significantly underestimated when holding one of these variables constant. Accurately quantifying these uncertainties is important for more detailed studies that commonly use crustal thickness,  $V_P$ , and  $V_S$  estimates derived from receiver function studies as a starting model.

## 2. Methods

### 2.1. Demonstration With Synthetic Data

We generate synthetic seismograms using the *raysum* forward modeling code for a plane wave impinging on a layered medium to demonstrate the ability of the autocorrelation technique to recover the reflectivity structure beneath a station (Frederiksen & Bostock, 2000). We used a simple  $\sim 1$ -Hz Gaussian source-time function to compute synthetic seismograms for a layer with a 30-km-thick crust,  $V_P = 6.2$  km/s, and  $V_P/V_S$  ratio of 1.75. The resulting  $S$ -wave conversion from the Moho ( $P_s$ ), Moho-reflected  $P$ -wave (Pmp), and later multiple phases (2P1S and 1P2S) are clearly observed in the modeled data (Figures 1a and 1b; naming convention follows Niu & James, 2002). The receiver functions for these waveforms were calculated using the time-domain iterative deconvolution method (Ligorria & Ammon, 1999) with a Gaussian alpha parameter of 2.8 ( $\sim 1$ -Hz center frequency; Figure 1c). The opposite polarities of the  $P$ -to- $S$  converted phases on

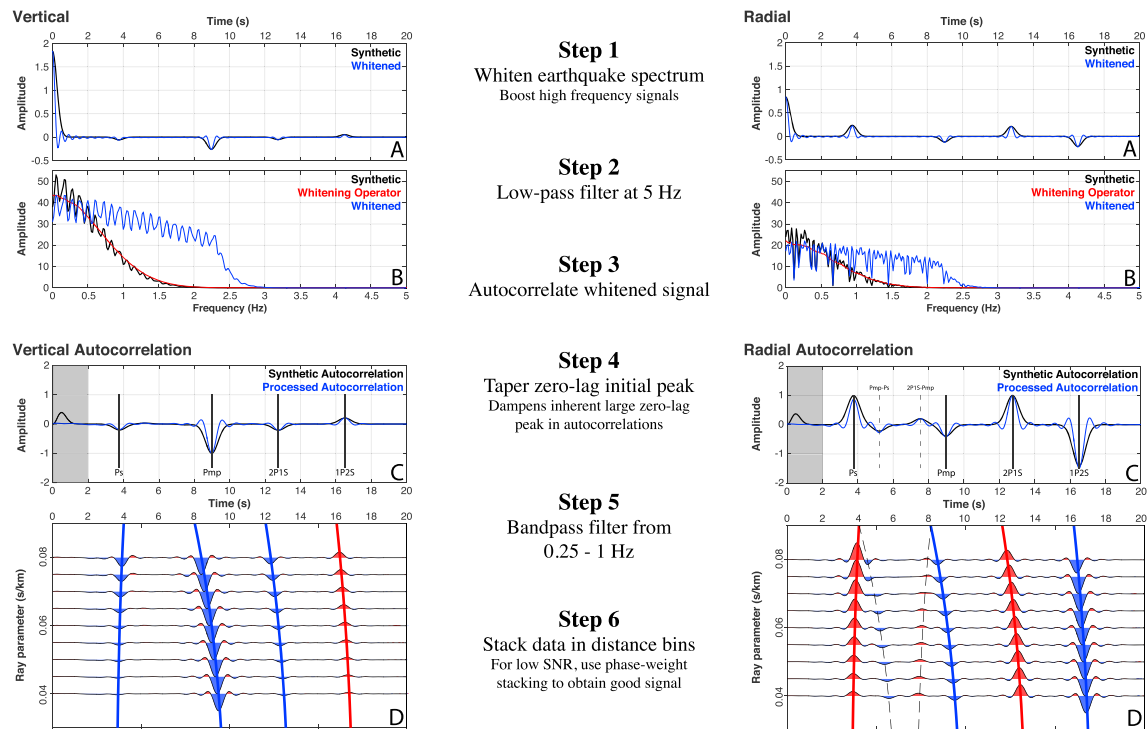


**Figure 2.** Autocorrelation processing using synthetic data. Seismograms correspond to the vertical (left) and radial (right) components of the synthetic data for a ray parameter of 0.06 s/km. (a) Synthetic seismogram (black) and resulting seismogram after spectral whitening (blue). (b) To whiten the spectrum, the spectrum of the synthetic data was divided by the smoothed spectrum (black divided by red line). Resulting spectrum shown in blue. (c) Comparison between autocorrelations from the synthetic data with (blue) and without (black) processing and locations of expected phases for a ray parameter of 0.06 s/km. A cosine taper is applied to the first 2 s of the autocorrelation to suppress the large amplitude at zero time lag (shaded). Amplitudes of waveforms are normalized. (d) Autocorrelations showing the recovery of various phases on the vertical and radial components. While this synthetic model uses a simple Gaussian source-time function, a zero-phase wavelet corresponding to depths to discontinuities would be recovered regardless of the complexity of the source-time function (as long as source-time function does not overlap in time with discontinuities). Dashed lines on radial autocorrelation represent spurious arrivals in the “correlation wavefield” (Phm et al., 2018). SNR = signal-to-noise.

the vertical and radial components result in large signals in the receiver functions after deconvolution; however, the similarity of the backscattered *P*-wave reflected off of the Moho on both components cancels during deconvolution.

To compute autocorrelation functions, we largely follow the processing steps outlined by Pham and Tkalčić (2017; Figure 2). Synthetic vertical and radial component data were resampled to 20 samples per second, and the spectra were whitened by dividing the original spectra by the smoothed spectra. The smoothed spectra was computed by taking a moving average in the frequency domain over a width of 0.34 Hz. The width of the frequency band for the spectral whitening operator can have a significant effect on the computed autocorrelations and is largely qualitative. We discuss the effects of different whitener widths in supporting information Text S2 and Figures S3 and S4. After spectral whitening, we apply a low-pass filter at 5 Hz and compute the autocorrelation of the vertical and radial components. We only need to consider one side of the autocorrelation, as it is symmetric around zero time lag. A cosine taper was applied to the first 2 s of the positive time lags of the autocorrelation to suppress the inherent high amplitude wavelet around zero time lag, and the waveform was then band-pass filtered between 0.25- to 1-Hz. This resulted in an autocorrelation function that has similar frequency content as the computed receiver functions.

The autocorrelation recovers all expected phases observed on the transmitted wavelet, as well as some spurious arrivals not present in the transmitted response (Figure 2d, right). Similar spurious wavelets have been observed in other studies and can be thought of as part of the correlation wavefield (e.g., Pham et al., 2018). These phases arise due to the correlation of the Pmp phase with other converted phases, namely, the Ps and

1P2S phases in this case, and the timing of these phases can be predicted by the difference between the correlated wave arrivals (Text S3 and Movie S1). These phases are present on both the vertical and radial autocorrelations but tend to be larger on the radial autocorrelation due to the similar amplitude of the Pmp arrival with other phases on the radial component.

## 2.2. $H$ - $\kappa$ Stacking

Using the  $P$ -to- $S$  conversions on receiver functions, we can apply  $H$ - $\kappa$  stacking analysis to solve for depths to discontinuities ( $H$ ) and their associated  $V_P/V_S$  ratio ( $\kappa$ ) in a layer (Zhu & Kanamori, 2000).  $H$ - $\kappa$  stacking is a widely used approach that predicts the timing of converted phases over a range of  $H$  and  $V_P/V_S$  space for different ray parameters and sums the receiver function amplitudes at the predicted times to find where conversion amplitudes are maximized. The equations for the travel times of the converted phases relative to the  $P$ -wave arrival time are given by

$$t_{PS} = H \left( \sqrt{\frac{1}{V_S^2} - p^2} - \sqrt{\frac{1}{V_P^2} - p^2} \right), \quad (1)$$

$$t_{2P1S} = H \left( \sqrt{\frac{1}{V_S^2} - p^2} + \sqrt{\frac{1}{V_P^2} - p^2} \right), \quad (2)$$

$$t_{1P2S} = 2H \sqrt{\frac{1}{V_S^2} - p^2}, \quad (3)$$

where  $H$  is the layer thickness,  $V_S$  is the shear wave velocity,  $V_P$  is the  $P$ -wave velocity, and  $p$  is the ray parameter (Zandt et al., 1995). This system of equations is linearly dependent, having three unknowns ( $H$ ,  $V_P$ , and  $V_S$ ) but only two independent equations (e.g.,  $t_{PS} + t_{2P1S} = t_{1P2S}$ ). Thus, to apply  $H$ - $\kappa$  stacking analysis, one of these parameters is commonly assumed. Given the relatively low trade-off of  $P$ -wave velocity with layer thickness ( $\Delta H = \frac{\partial H}{\partial V_P} \Delta V_P \sim 5 \Delta V_P$  km), the  $P$ -wave velocity in the layer of interest is generally the assumed parameter (Zhu & Kanamori, 2000).

To calculate the amplitudes using  $H$ - $\kappa$  analysis, the stacked amplitudes of the receiver functions within a particular bin are summed along the predicted moveout curves, represented by

$$s(H, k) = \sum_{n=1}^N \sum_{m=1}^M w_m r_{nm}, \quad (4)$$

where  $w$  is a weighting factor for  $M$  phases that will be included in the stacking analysis (commonly  $t_{PS}$ ,  $t_{2P1S}$ , and  $t_{1P2S}$ ), which includes the effects of polarity changes depending on phase (where the sum of the absolute values of  $w = 1$ ), and  $r$  is the amplitude of receiver functions stacked into  $N$  ray-parameter bins. The  $t_{1P2S}$  is not necessary to calculate  $V_P/V_S$  ratios due to its linear dependence with the other phases but can be added to contribute to the sum of the amplitudes to better constrain  $H$ - $\kappa$  space if it is a coherent arrival. In practice, the arrival associated with the  $t_{1P2S}$  phase tends to be weak or difficult to observe, as it arrives relatively late in the  $P$ -wave coda. The grid search results for  $H$ - $\kappa$  stacking using the  $t_{PS}$  and  $t_{2P1S}$  phases on the synthetic receiver functions (Figure 1c) are shown in Figure 3a.

## 2.3. Calculating Uncertainty

Calculating errors from  $H$ - $\kappa$  stacking analysis is not straightforward. Populations of “good” solutions were defined as solutions with amplitudes within the standard error of the maximum amplitude (e.g.,  $1 - \sigma_M = 1 - \sqrt{\frac{\sigma_r^2}{N}}$ , where  $N$  = the number of events in the stack; Eaton et al., 2006). While solution populations tend to be Gaussian-distributed over  $H$ - $\kappa$  space, the solution that produces the maximum amplitude does not need to be at the center of the Gaussian distribution. Thus, the solution and associated uncertainties cannot be properly characterized by the mean and standard deviation of the solution population. Therefore, to calculate the uncertainties from the  $H$ - $\kappa$  stacking results, we report the 15.9% and 84.1% quantiles of the solution population, which corresponds to middle 68.2% of solutions and is analogous to the standard deviation for Gaussian-distributed populations, while reporting the maximum amplitude as the preferred solution.

#### 2.4. Plotting in Parallel Coordinates

As  $H$ - $\kappa$  stacking only employs a grid search over two dimensions ( $H$  and  $\kappa$ ), the results are easy to visualize in two-dimensional space. However, an equivalent way to show the results of  $H$ - $\kappa$  stacking is through the use of parallel coordinates (Figure 3; Inselberg, 2009; Heinrich & Weiskopf, 2013). In this approach, solutions are plotted in parallel in one-dimensional space. We connect individual solutions by colored lines corresponding to the solution amplitude, which allows for the easy perception of trade-offs between parameters (Figure 3b). While the use of parallel coordinates is not necessary for visualizing two-dimensional results, this approach can be extended to  $N$ -dimensions, allowing us to easily visualize the solutions and trade-offs in higher-dimensional space.

#### 2.5. $H$ - $\kappa$ - $V_P$ Stacking

The addition of the autocorrelation allows for the recovery of the Moho-reflected  $P$ -wave (Pmp), which is strictly controlled by the thickness and  $V_P$  of the layer of interest (Figure 2). The timing of the Pmp phase can be predicted with the equation:

$$t_{\text{Pmp}} = 2H \sqrt{\frac{1}{V_P^2} - p^2}. \quad (5)$$

On inspection, one can see that this equation is still linearly dependent on  $t_{\text{Ps}}$  and  $t_{2\text{P1S}}$  (e.g.,  $t_{2\text{P1S}} - t_{\text{Ps}} = t_{\text{Pmp}}$ ), so obtaining the timing of this phase alone does not contribute independent information to help us constrain our three unknowns. For example, even in traditional receiver function studies, we could use the difference in arrival times between the  $t_{2\text{P1S}}$  and  $t_{\text{Ps}}$  phases to solve for the average  $P$  velocity in the layer. However, introducing the autocorrelation has two major advantages over solving for  $V_P$  using the receiver function arrivals: (1) The moveout of the  $t_{\text{Pmp}}$  phase is steeper than that of  $t_{\text{Ps}}$  and  $t_{2\text{P1S}}$  due to its independence of  $V_S$ , and (2) more importantly, the autocorrelation gives us a  $t_{\text{Pmp}}$  observation against which to check the validity of the result of the  $H$ - $\kappa$  stack. Thus, we can add terms to equation (4) from the autocorrelations that help constrain the solution in  $H$ - $\kappa$ - $V_P$  space following similar lines of logic as adding the redundancy of the  $t_{1\text{P2S}}$  phase in  $H$ - $\kappa$  stacking analysis. The generalized equation, which can be used to sum over all phases of interest in the receiver functions and autocorrelations, is

$$s(H, \kappa, V_P) = \sum_{l=1}^L \left( \sum_{i=1}^M w_i \tilde{r}_{il} + \sum_{j=1}^N w_{M+j} \tilde{Z}_{jl} + \sum_{k=1}^O w_{M+N+k} \tilde{R}_{kl} \right), \quad (6)$$

where  $w$  is a weighting factor for  $M + N + O$  phases that will be included in the stacking analysis from the receiver functions, vertical autocorrelations, and radial autocorrelations (where the sum of the absolute values in  $w = 1$ ),  $\tilde{r}$ ,  $\tilde{Z}$ , and  $\tilde{R}$  are the stacked amplitudes of the receiver functions and autocorrelations in  $L$  ray-parameter bins normalized to the maximum stacking amplitude for that data set (i.e., the maximum amplitude contribution from each data set is equal to the corresponding weight for that data set). In this study, we do not include the radial autocorrelation in the  $H$ - $\kappa$ - $V_P$  stacking analysis, as the Pmp phase on the radial autocorrelation has a relatively low amplitude and may be contaminated by the spurious arrivals of the correlation wavefield, while the  $S$ -wave converted energy (Ps, 2P1S, and 1P2S phases) is usually more apparent on the receiver functions than on the radial autocorrelations (Figure 2b). However, they could be included in stacking if apparent in the data. The amplitude of the  $t_{\text{Pmp}}$  phase is negative on both the vertical and radial autocorrelations, so this sum must be subtracted to positively contribute to the  $H$ - $\kappa$ - $V_P$  stacking amplitude, which we account for implicitly in the weighting vector in equation (6). Since we exclude the radial autocorrelation and all  $P$ -s converted phases on the vertical autocorrelation, equation (6) is simply the stacked amplitude of the  $t_{\text{Ps}}$  and  $t_{2\text{P1S}}$  phase in the receiver functions ( $M = 2$ ) and the  $t_{\text{Pmp}}$  phase from the vertical autocorrelation ( $N = 1$ ). For simplicity,  $s(H, \kappa, V_P)$  is also normalized so that the maximum value of the stack equals one.

We applied the  $H$ - $\kappa$ - $V_P$  stacking algorithm using a weighting of 0.4 and 0.2 for the receiver function Ps and 2P1S phase and 0.4 for the autocorrelation Pmp phase to the synthetic data for comparison with  $H$ - $\kappa$  results. As with  $H$ - $\kappa$  stacking, the solution that resulted in the maximum stacking amplitude was taken as the best solution, and uncertainties in the  $H$ - $\kappa$ - $V_P$  stacking solutions were calculated in the same way as described in section 2.2. Visualizing the results and trade-offs between  $H$ ,  $\kappa$ , and  $V_P$  in Cartesian three-dimensional space

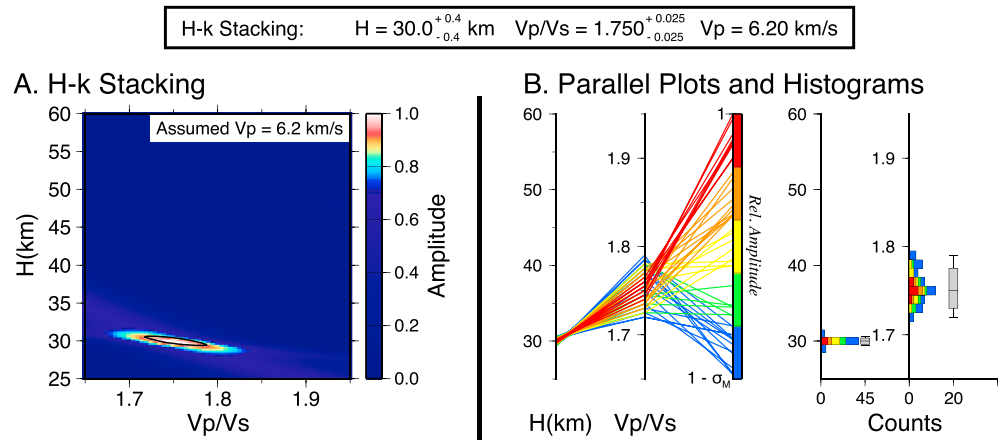


**Figure 3.**  $H$ - $\kappa$  stacking analysis for synthetic data shown in equivalent representations of  $H$ - $\kappa$  parameter space. Solutions for  $H$ - $\kappa$  stacking analysis at top. Synthetic data were created using  $H = 30$  km,  $V_p/V_s = 1.75$ ,  $V_p = 6.2$  km/s. Assumed  $V_p$  for stacking was 6.2 km/s. (a) Typical representation of  $H$ - $\kappa$  grid search with 2-D surface colored by relative stacking amplitude. Black contour represents solutions within the standard error of the maximum stacking amplitude. (b: left)  $H$ - $\kappa$  solutions shown using parallel coordinates. Lines are colored by relative amplitude and are connected to show correlations. All solutions are within the standard error of the maximum stacking amplitude. (b: right) Histogram of solutions colored by relative amplitude. Box and whisker plots show maximum amplitude (middle line) and middle 68.2% of the population distribution (box) along with the range of the “good” solutions (whiskers).

is not particularly helpful in gaining an intuitive understanding solution space, but is rather straightforward when viewed in parallel coordinates (Figure 4).

$H$ - $\kappa$ - $V_p$  stacking has similar shortcomings as  $H$ - $\kappa$  stacking; it works best on homogenous layers with flat discontinuities where the highest amplitudes match the predicted moveouts of the respective phases. However, introducing the amplitude information from the autocorrelations allows for the validation of the average  $P$ -wave velocity in a layer and constrains the  $H$ - $\kappa$  solution through decreasing the overall stacking amplitude if

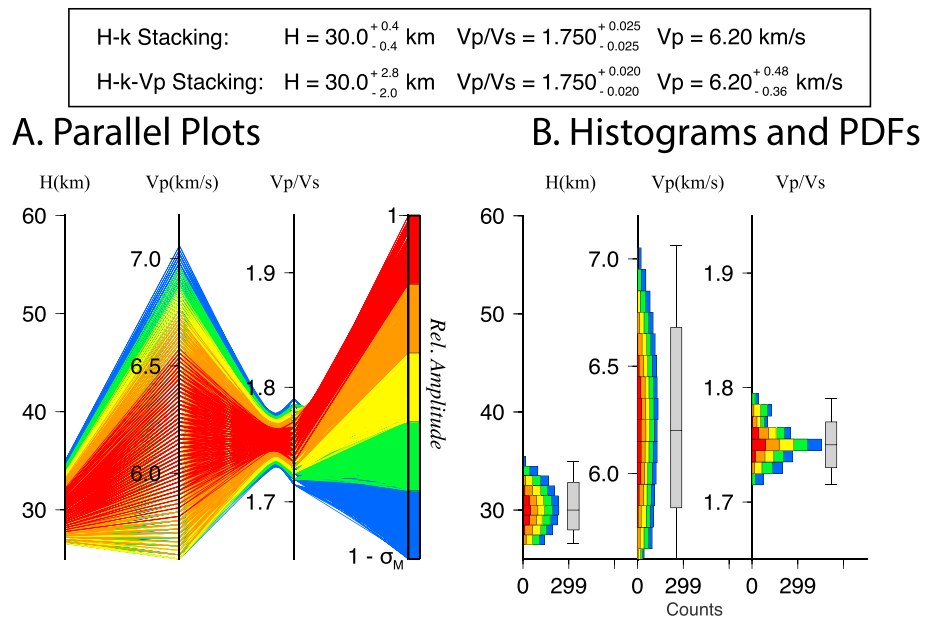


**Figure 4.** (a) Parallel plot of  $H$ - $\kappa$ - $V_p$  solutions for synthetic data. Solution sets are colored by amplitude to show trade-offs between various parameters. (b) Histogram of solutions colored by relative amplitude. Box and whisker plots show maximum amplitude (middle line) and middle 68.2% of the population distribution (box) along with the range of the “good” solutions (whiskers).

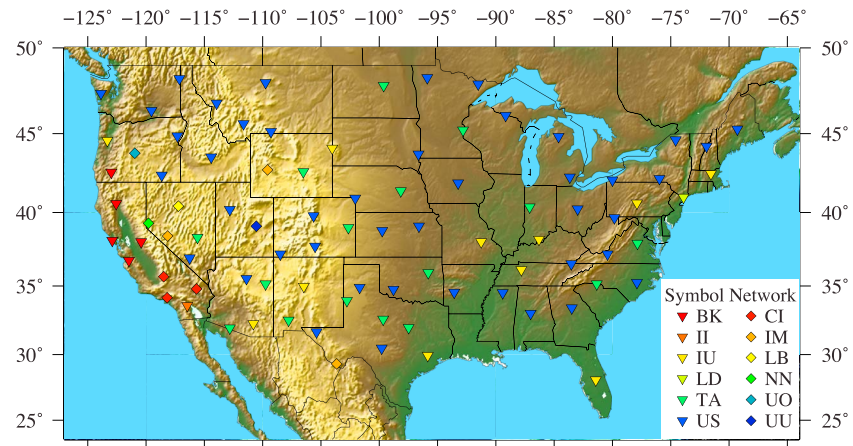


**Figure 5.** The U.S. Reference Network stations that were analyzed as part of this study. Networks denoted by colors and shapes.

the Pmp arrival is not observed on the autocorrelation. The relatively low trade-off between  $H$  and  $V_P$  allows a significant portion of  $V_P$  space to fall within the solution bounds (Figure 4); however, while uncertainties in  $V_P$  may be large, they are at least constrained by data rather than by simple assumptions about  $V_P$  based on geographic region or a priori assumptions (e.g., EARS, Crotwell & Owens, 2005; Crust1.0, Laske et al., 2013). Adding the  $V_P$  parameter also gives us more meaningful uncertainties in our  $H$  and  $V_P/V_S$  estimates, as uncertainties in these parameters as a function of changes in  $V_P$  are unquantified in typical  $H$ - $\kappa$  stacking analysis. The effects of  $V_P$  uncertainty on the uncertainties of  $H$  and  $V_P/V_S$  can be seen when comparing the results of the  $H$ - $\kappa$  and  $H$ - $\kappa$ - $V_P$  stacking (Figures 3 and 4).

### 3. Application to USArray Data

#### 3.1. Data

We apply the above approach to data from the transportable array (TA) reference network ([ds.iris.edu/mda/\\_US-REF](https://ds.iris.edu/mda/_US-REF)). We analyzed data from 1,347 Mw  $\geq 6$  earthquakes occurring at 30–95 epicentral degrees away from 88 TA reference stations between the years of 2000 and 2017 (Figure 5). These stations are from the long running (>10 years) backbone network designed to provide a continental reference for the 18-month deployment of most USArray TA stations. Initially, the seismograms were rotated into ZRT components and filtered from 0.05 to 9 Hz. Data were then visually inspected, and records that did not show a clear  $P$ -wave arrival on the vertical component at a station were discarded before further analysis.

#### 3.2. Receiver Functions

Quality-controlled radial and vertical seismograms were used to calculate receiver functions using the time-domain iterative deconvolution method (Ligorria & Ammon, 1999) with a Gaussian alpha parameter of 2.8 (~1-Hz center frequency), resulting in a total computation of 29,847 receiver functions. We removed any receiver functions whose fit to the observed radial component seismogram after convolution of the receiver function and the vertical component seismogram was <80%. These imply inconsistency between the receiver function and the observed data, generally resulting from low signal-to-noise ratios in the vertical and radial components. Computed receiver functions were further manually inspected using the Funclab software package (Eagar & Fouch, 2012; Porritt & Miller, 2018) to remove traces that showed structure inconsistent with other computed receiver functions at a particular station or that recovered unrealistic Earth structure. Receiver functions were then separated into 10 ray-parameter bins (0.038–0.082 s/km at 0.0055 s/km per bin) due to the different moveouts of the phases of interest and linearly stacked.

#### 3.3. Autocorrelations

We apply the autocorrelation processing steps summarized in Figure 2 to the vertical and radial components of the waveforms that resulted in high-quality receiver functions. An example of the processing steps and

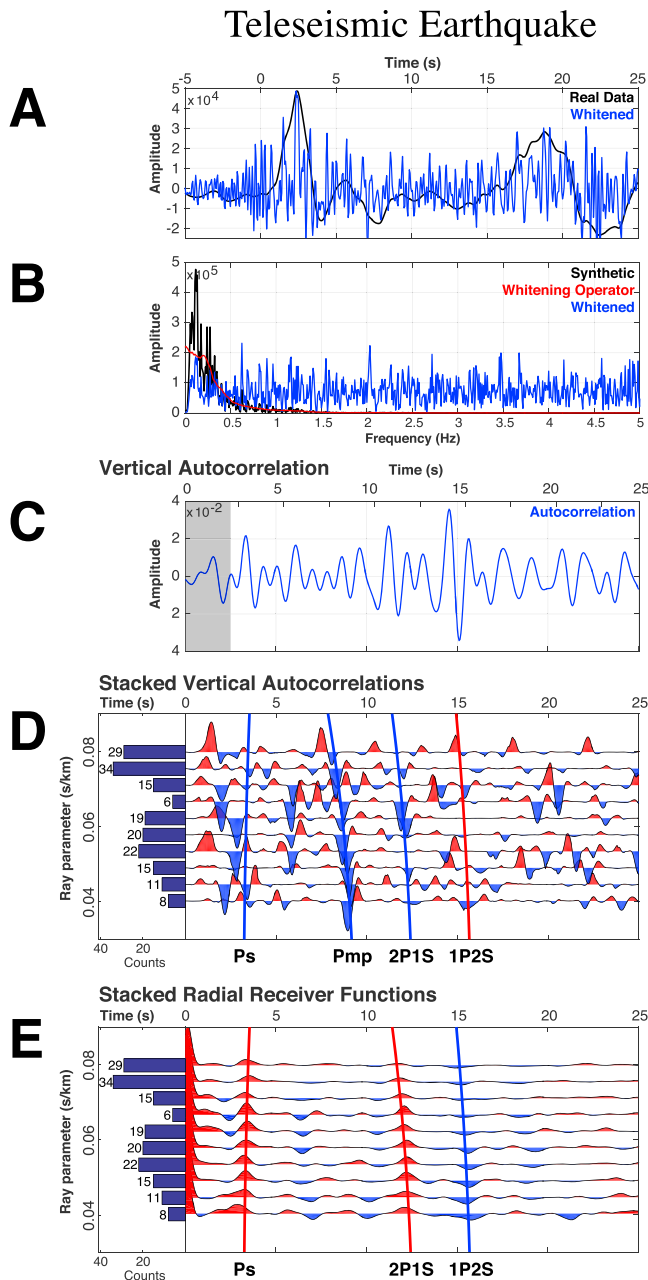


**Figure 6.** Processing steps applied to station IU.HRV.00 located in Massachusetts. (a) A vertical component record of a teleseismic earthquake filtered at 0.025–9 Hz (black) compared to spectrally whitened earthquake signal (blue). Amplitude of whitened signal normalized to nonwhitened signal for plotting. (b) Spectrum of observed teleseismic earthquake (black), whitening operator calculated with a 0.34-Hz moving average width (red), and the resulting whitened spectrum (blue). (c) Autocorrelation of whitened earthquake signal (blue in (a)). (d) Binned and phase-weight stacked autocorrelations for 179 events recorded at IU.HRV.00. Moveout curves for Ps, Pmp, 2P1S, and 1P2S are shown for a model with  $H = 27.8$  km,  $V_P = 5.96$  km/s, and  $V_P/V_S = 1.69$ . Curves are colored by polarity of expected arrival (blue = negative and red = positive). (e) Linearly stacked receiver functions station IU.HRV.00 (same events as used to calculate autocorrelations).

results for real data is shown in Figure 6. Spectral whitening over a 0.34-Hz moving average window was applied to the spectrum of the earthquakes to boost high-frequency energy, and the resulting seismogram was low-pass filtered at 5 Hz. The autocorrelation of the resulting waveforms was then computed for each event at each station and band-pass filtered between 0.25 and 1 Hz. Prior to computing the autocorrelations, we also applied sign-bit temporal normalization to seismograms after spectral whitening, as has been used by autocorrelation studies using ambient noise (Oren & Nowack, 2017; Tibuleac & von Seggern, 2012). In general, we find that autocorrelations without sign-bit temporal normalization produce better results for earthquake-based autocorrelations (Figure 7).

In practice, the narrow band of the filter and relatively low amplitude of the Pmp arrival makes this phase difficult to recover. Only in high-quality data with a large number of events can a clear Pmp phase be observed on the vertical autocorrelations after linear stacking in different ray-parameter bins. We therefore show phase-weight stacking to enhance the clarity of the Pmp phase (Figure 7). Phase-weight stacking is a non-linear stacking method that enhances the “in-phase” signals associated with low signal-to-noise ratio arrivals (Pham & Tkalčić, 2017; Schimmel & Paulssen, 1997). The strength of the nonlinearity of the phase-weighted stack is controlled by an exponential term,  $\eta$ , which when zero is equivalent to a linear stack and becomes stronger at higher values. For this study, we use an  $\eta$  of 2. Autocorrelation signals were downsampled to 10 samples per second prior to phase-weight stacking to create smoother stacks. This downsampling does not change the character of the waveforms, as they have been filtered with a high-frequency corner of 1 Hz. Other passbands were investigated as well (0.125–1 Hz, 0.25–2 Hz, and 0.125–2 Hz) and were stacked using both linear and non-linear approaches. These results are similar to the 0.25- to 1-Hz passband (Figures S1 and S2).

### 3.4. $H$ - $\kappa$ - $V_P$ stacking

We applied  $H$ - $\kappa$ - $V_P$  stacking to linearly stacked 1-Hz receiver functions and vertical-component autocorrelations. The weights used to sum the different phases were generally 0.4 and 0.2 for receiver function Ps and 2P1S and 0.4 for vertical autocorrelation Pmp but were adjusted depending on the clarity of the phases. All ray-parameter bins with data present were given equally weighted contributions in the stacking procedure. The grid search range for  $H$ ,  $V_P/V_S$ , and  $V_P$  was generally 25–60 km, 1.65–1.95, and 5.6–7.2 km/s in steps of 0.2 km, 0.005  $V_P/V_S$ , and 0.02  $V_P$ . While the choice of the grid search range be subjective, it is important to choose bounds that encompass realistic solutions to crustal properties given the geologic context of an individual station. The step size for each parameter is also subjective but needs to be fine enough to accurately represent model space, which is important for constraining uncertainties in the final results. This selection can be validated by using histograms of each parameters to ensure that solution populations have a more-or-less Gaussian distribution. Solutions for each station were visually inspected and validated by plotting the predicted arrival times from the solutions within the standard error of the maximum on the binned receiver function and phase-weight stacked autocorrelation results, as the Pmp phase is generally clearer on the phase-weighted stacks than on the linear stacks. At stations where robust solutions were observed near the bounds of the grid search, the grid search range was adjusted accordingly. It is important to note that performing  $H$ - $\kappa$ - $V_P$

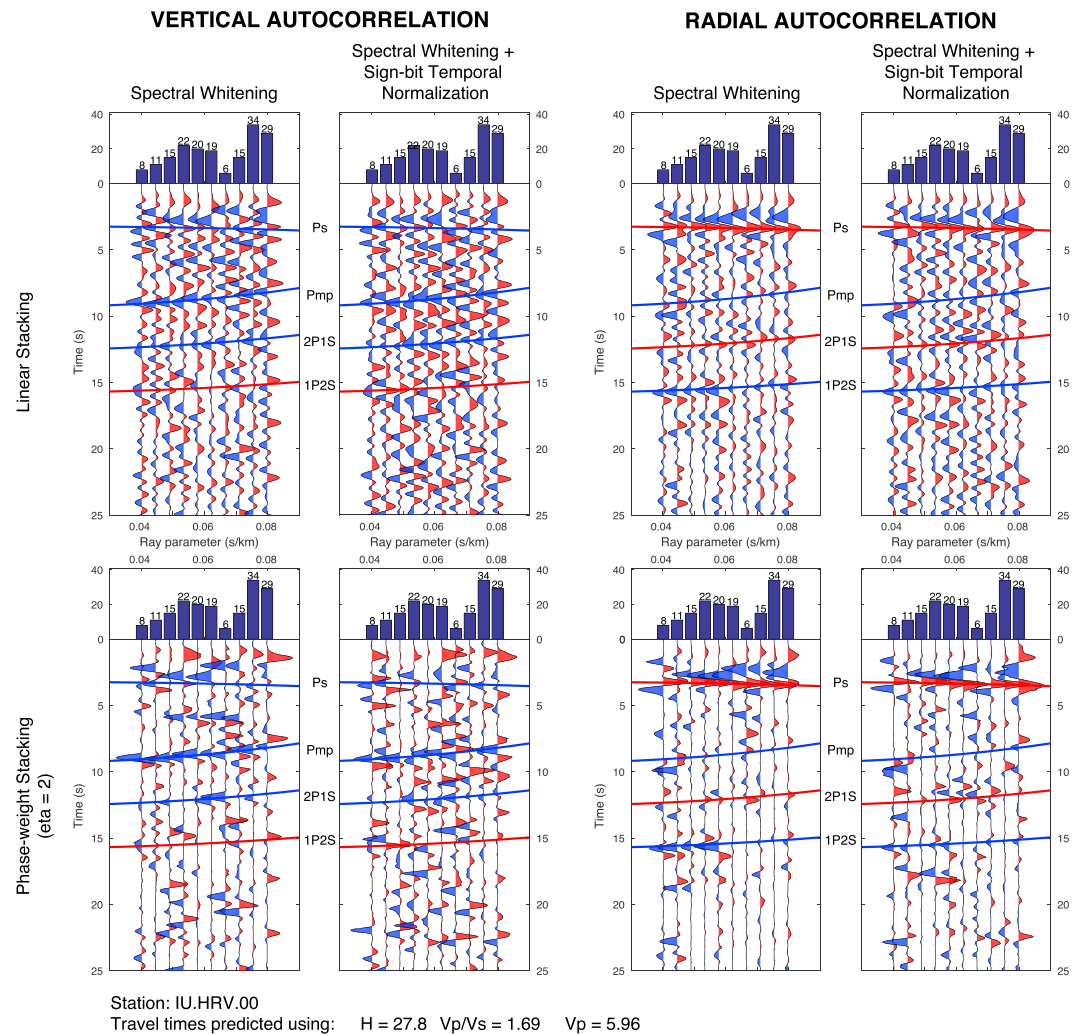


**Figure 7.** Comparison of linearly and phase-weight stacked vertical and radial autocorrelations for station IU.HRV.00 with and without sign-bit temporal normalization during “Step 1” in Figure 5. Autocorrelations are band-pass filtered from 0.25 to 1 Hz. We find that the signals of interest are most apparent in the phase-weight stacked autocorrelations without sign-bit normalization, likely due to the preservation of wavelet shape and relative amplitude information.

stacking on phase-weight stacked autocorrelations can produce different results, as frequency distortion and phase shifts can occur as a result of the nonlinear stacking. Therefore, we prefer to use the phase-weighted stacks only to visually validate the  $H\text{-}\kappa\text{-}V_P$  results from the linearly stacked data. We also apply  $H\text{-}\kappa$  stacking to the receiver function data at each station for comparison using an assumed  $V_P$  of 6.2 km/s over the same  $H$  and  $V_P/V_S$  range as for  $H\text{-}\kappa\text{-}V_P$  stacking analysis.

### 3.5. Gaussian Mixture Modeling

In some cases, multiple local maxima in  $H\text{-}\kappa\text{-}V_P$  space are observed. In order to calculate the appropriate error envelope for the individual solutions, the solution families must be separated. We use Gaussian Mixture Modeling (GMM) to separate out different sets of solutions (McLachlan & Peel, 2004).

GMM is a generative distribution-based unsupervised pattern recognition, or “cluster analysis,” algorithm. GMM differs from  $k$ -means clustering (Arthur & Vassilvitskii, 2007; Lloyd, 1982) in that it assumes that the solutions are Gaussian distributed in model space rather than splitting model space into Voronoi cells

as in  $k$ -means algorithms. GMM is somewhat similar to  $k$ -means clustering in that it looks to minimize the Euclidean distance between individual data points and “ $k$ ” centroid locations, where  $k$  is a user-defined number of groups, but differs in that it normalizes the Euclidean distance by the covariance matrix, thus maintaining sensitivity to trade-offs between parameters.

To find the centroids in model space, an expectation-maximization algorithm is applied (Dempster et al., 1977). This is an iterative, stochastic algorithm that places  $k$  Gaussian-shaped centroids consisting of a mean and standard deviation in data space, calculates probabilities that data points lie within this Gaussian pulse, and perturbs the centroids until the joint probability distribution of the data and centroid locations are maximized. As solution populations in  $H$ - $\kappa$  and  $H$ - $\kappa$ - $V_P$  spaces naturally cluster into Gaussian distributions, GMM clustering is very effective at accurately separating out groups of solutions. To find  $k$ ,  $H$ - $\kappa$ - $V_P$  results were visually inspected using parallel coordinate plots.

## 4. Results

### 4.1. Single Station Examples

The clarity and quality of the autocorrelation results at individual stations generally coincide with stations that returned good receiver function results. Below, we show some representative examples of stations of different quality and compare their results from  $H$ - $\kappa$ - $V_P$  stacking analysis with those from  $H$ - $\kappa$  stacking analysis, as well as with other studies.

Station IU.HRV.00 in Massachusetts represents one of the best solutions in this data set, having clear Pmp, Ps, 2P1S, and 1P2S phases (although 1P2S did not contribute to the stacking analysis). The  $H$ - $\kappa$ - $V_P$  stacking results do not significantly differ from those obtained by  $H$ - $\kappa$  stacking analysis (Figure 8), as the Ps and 2P1S arrivals that produce the maximum amplitude in the  $H$ - $\kappa$  (black dashed line) and  $H$ - $\kappa$ - $V_P$  stacking analysis (colored lines) are identical. Introducing the Pmp phase, however, shows that the assumed  $V_P$  for  $H$ - $\kappa$  stacking of 6.2 km/s is slightly too fast compared to the  $\sim$ 6.0 km/s average  $V_P$  obtained from  $H$ - $\kappa$ - $V_P$  stacking. This relatively small change in  $V_P$  also effects the estimates of  $V_P/V_S$  ratio by 0.02, resulting in an overestimation of crustal thickness by 1.6 km, or 6% when relying only on  $H$ - $\kappa$  stacking.

At other stations, introducing the Pmp phase can result in large changes in the other parameters, even if the assumed  $V_P$  is relatively close to the true value. For example, station US.NLWA located in the Pacific Northwest shows a very clear Pmp phase resulting in a recovered  $V_P$  of 6.24 km/s (Figure 9). While only negligibly different than the assumed  $V_P$  in  $H$ - $\kappa$  stacking (6.2 km/s), the constraint of the timing of the Pmp phase results in a rather large change in the estimated  $V_P/V_S$  ratio from 1.66 to 1.74 (corresponding to a decrease in  $V_S$  of 150 m/s) and a thinning of the crustal thickness estimate by 1.4 km. One can see that there is no observable Pmp phase associated with the  $H$ - $\kappa$  stacking solution of  $H = 25.6$  km and  $V_P/V_S = 1.66$  assuming a  $V_P$  of 6.2 km/s in the autocorrelations (Figure 9, black dashed line). The resulting estimate of average crustal  $V_S$  based on the  $H$ - $\kappa$ - $V_P$  stacking solution ( $V_S = 3.58$  km/s) is also more consistent with studies that utilize the sensitivities of surface wave dispersion data in this area to constrain crustal shear velocity ( $\sim$ 3.3 km/s, Schmandt et al., 2015;  $\sim$ 3.5 km/s, Delph et al., 2018) than the  $H$ - $\kappa$  solution ( $V_S = 3.73$  km/s).

Some stations show much more complicated results than these relatively simple and high-quality examples, exhibiting multiple solutions that must be separated by cluster analysis. Station US.GOGA.00 shows an example of where GMM is necessary to separate out solutions in  $H$ - $\kappa$ - $V_P$  space in order to calculate meaningful uncertainties (Figure 10). On visual inspection of the parallel plot (Figure 10c), it is clear that two solution families exist: a thicker, high  $V_P$ , and low  $V_P/V_S$  solution (pink) and thinner, low  $V_P$ , and higher  $V_P/V_S$  solution (purple). While the thinner solution has higher stacking amplitudes overall, a clear 2P1S phase is not seen for this solution (Figure 10b, purple lines  $\sim$ 14 s). Thus, the bulk crustal properties beneath the station are likely more accurately represented by the thicker solution. This solution ( $H = 43.6$  km,  $V_P = 6.86$  km/s) is also much closer to the thickness and  $P$ -wave velocity estimates from wide-angle reflection data in this region ( $H = 37$ – $39$  km and  $V_P = 6.5$ – $6.6$  km/s; Hawman et al., 2012) than the alternative solution ( $H = 30.0$  km,  $V_P = 5.76$  km/s). Thus, as with  $H$ - $\kappa$  stacking analysis, results of  $H$ - $\kappa$ - $V_P$  stacking analysis can be non-unique and may require outside context to obtain the most likely estimate when multiple solutions exist or the result is ambiguous.

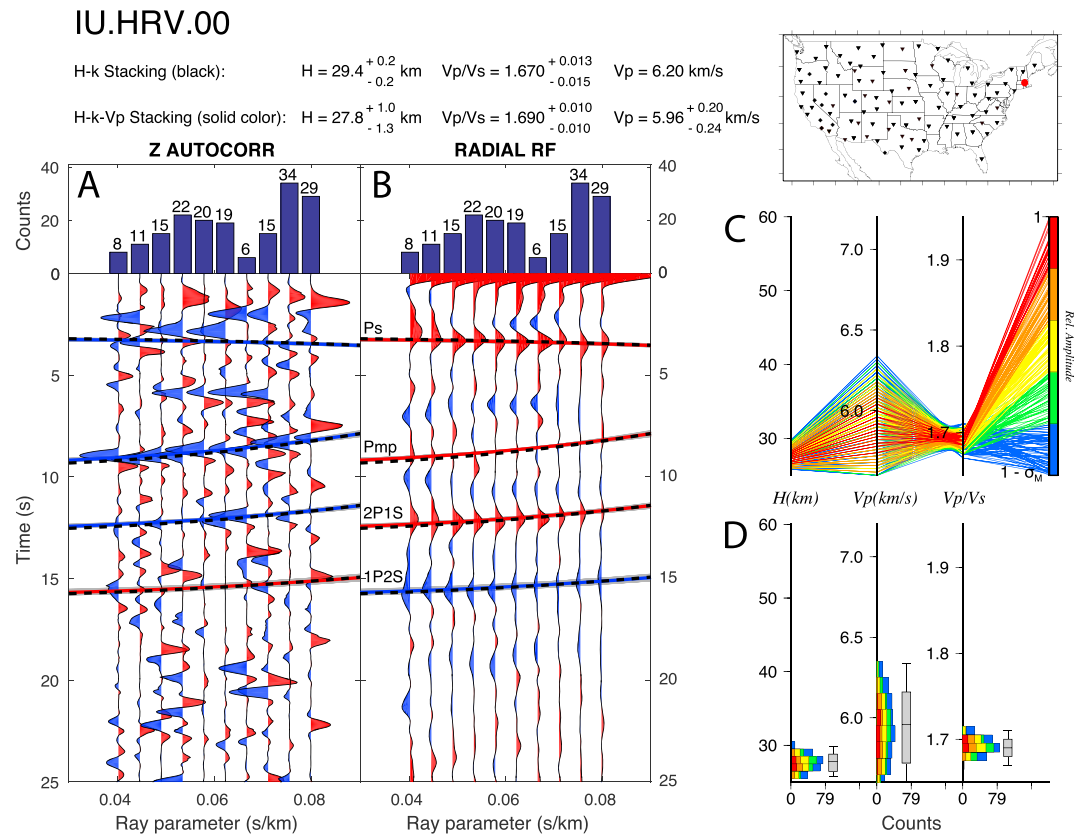


**Figure 8.** Analysis of station IU.HRV.00 located in Massachusetts (red dot on map). Results from  $H\text{-}\kappa$  and  $H\text{-}\kappa\text{-}V_P$  stacking analysis shown at the top. Predicted travel times for different phases calculated from the  $H\text{-}\kappa\text{-}V_P$  stacking analysis solution are colored by expected polarity of that phase (red = positive and blue = negative) on (a,b). Gray lines represent prediction from solutions within the standard error of the maximum stacking amplitude. Black dashed lines represent solution from  $H\text{-}\kappa$  stacking analysis. (a) Vertical autocorrelations. (b) Radial receiver functions. (c) Parallel plot of  $H\text{-}\kappa\text{-}V_P$  solutions colored by relative amplitude. (d) Histogram of solutions colored by relative amplitude. Box and whisker plots show maximum amplitude (middle line) and middle 68.2% of the population distribution (box) along with the range of the “good” solutions (whiskers).

A similar inspection was done for all stations analyzed to verify that the  $H\text{-}\kappa\text{-}V_P$  solutions were associated with visible phases in the waveforms, and all results were compared to the  $H\text{-}\kappa$  stacking solutions at the same station (Figure S6). If multiple families of solutions were observed in the data, GMM cluster analysis was performed to obtain the most likely solution and associated uncertainties. The parameters used for stacking results (e.g., grid search range and weighting for individual phases) and solutions for each station can be found in Table S1.

#### 4.2. Comparison With Existing Models

The combined autocorrelation and receiver function results provide a relatively coarse background model of crustal properties (thickness, average  $V_P$ , and average  $V_S$ ) for the conterminous United States. We compare our estimates of thickness and  $P$ -wave velocity with Crust1.0 (Laske et al., 2013; Figure 11). Crust1.0 is a  $1^\circ \times 1^\circ$  global model of crustal characteristics that uses crustal thickness estimates from receiver function and active source studies and infers average crustal  $V_P$  from the geologic context of a region and a global sediment thickness model. We also compare crustal thickness estimates with a model created from the multi-mode stacking of  $P$ -wave receiver functions on USArray data and our  $V_S$  (or  $V_P/\kappa$ ) estimates to the average vertical  $V_S$  of the crust based on this thickness (Schmandt et al., 2015). To compare these 2-D surfaces with our single-station results, we simply extract the result from the nearest grid point in each model to our stations.

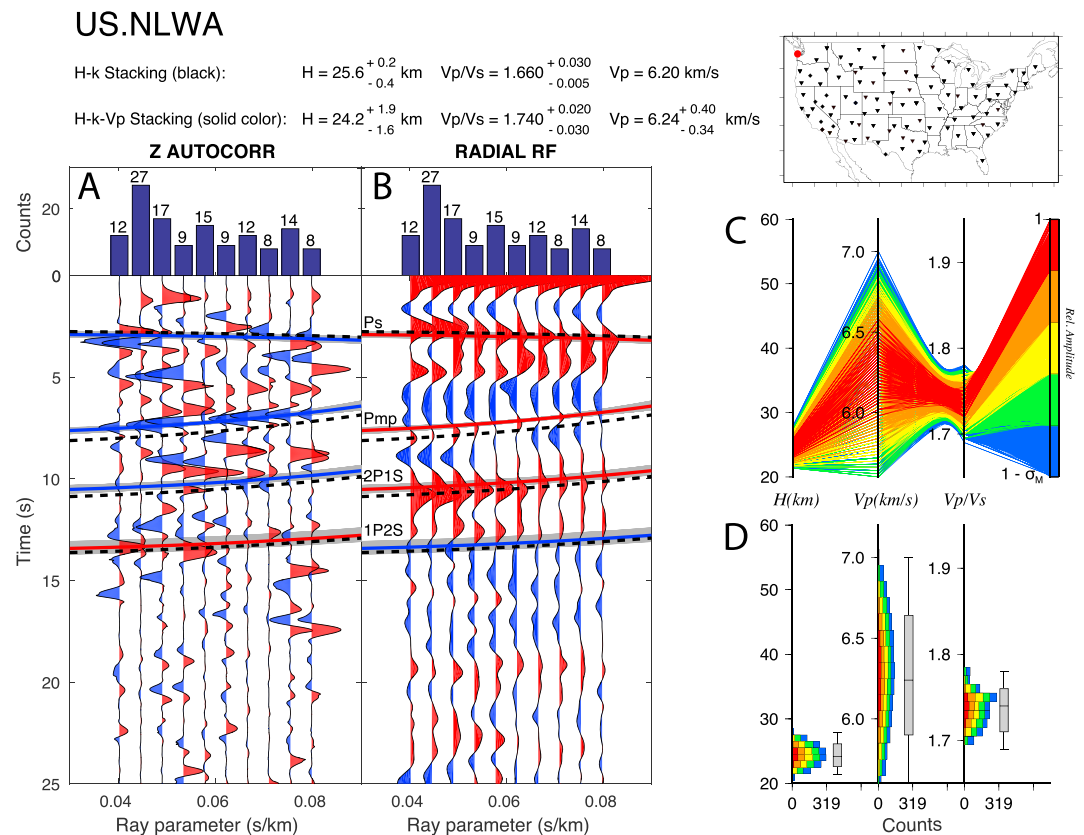


**Figure 9.** Analysis of station US.NLWA located at Neilton Lookout, Washington (red dot on map). Results from  $H$ - $\kappa$  and  $H$ - $\kappa$ - $V_p$  stacking analysis shown at the top. Predicted travel times for different phases calculated from the  $H$ - $\kappa$ - $V_p$  stacking analysis solution are colored by expected polarity of that phase (red = positive and blue = negative) on (a,b). Gray lines represent prediction from solutions within the standard error of the maximum stacking amplitude. Black dashed lines represent solution from  $H$ - $\kappa$  stacking analysis. (a) Vertical autocorrelations. (b) Radial receiver functions. (c) Parallel plot of  $H$ - $\kappa$ - $V_p$  solutions colored by relative amplitude. (d) Histogram of solutions colored by relative amplitude. Box and whisker plots show maximum amplitude (middle line) and middle 68.2% of the population distribution (box) along with the range of the “good” solutions (whiskers).

In general, the pattern of crustal thickness variations are similar to other models, with thin crust through most of the western United States and along the coastal plains of the southern and eastern United States (Figure 11a). The root-mean-square difference between the crustal thickness estimates from our model and the models of Crust1.0 and Schmandt et al. (2015) are 5.75 and 5.49 km, with 65% of our results falling within 5 km of these models (shown for Crust1.0; Figure 11b). Of course, it is difficult to compare these datasets directly as they are based on different data, methodologies, and assumptions. Our model, however, has an advantage in that we obtain uncertainties alongside these estimates.

We also compare our  $V_p$  results with those embedded within the Crust1.0 model, which is largely based on the average velocity characteristics of different tectonic and geologic domains from active source data (Figure 11c). Our results show a considerably wider range of average crustal  $V_p$  compared to the relatively narrow range predicted by Crust1.0 in the conterminous United States (Figure 11d). Disagreement between our  $V_p$  results and those from Crust1.0 could be explained by the relatively weak strength of the Pmp phase in autocorrelations at many stations. This could be due to relatively small changes in  $V_p$  across the Moho depending on tectonic region or to backazimuthal variations in Moho depth and velocity structure beneath a station that lead to deviations from the inherent 1-D assumption in  $H$ - $\kappa$  and  $H$ - $\kappa$ - $V_p$  stacking analysis. Also, oversimplifications to velocity variations within different tectonic domains in Crust1.0 or the fundamentally different sensitivities of the datasets used to constrain crustal properties in Crust1.0 (mainly active source data) likely also contribute to the disagreement.

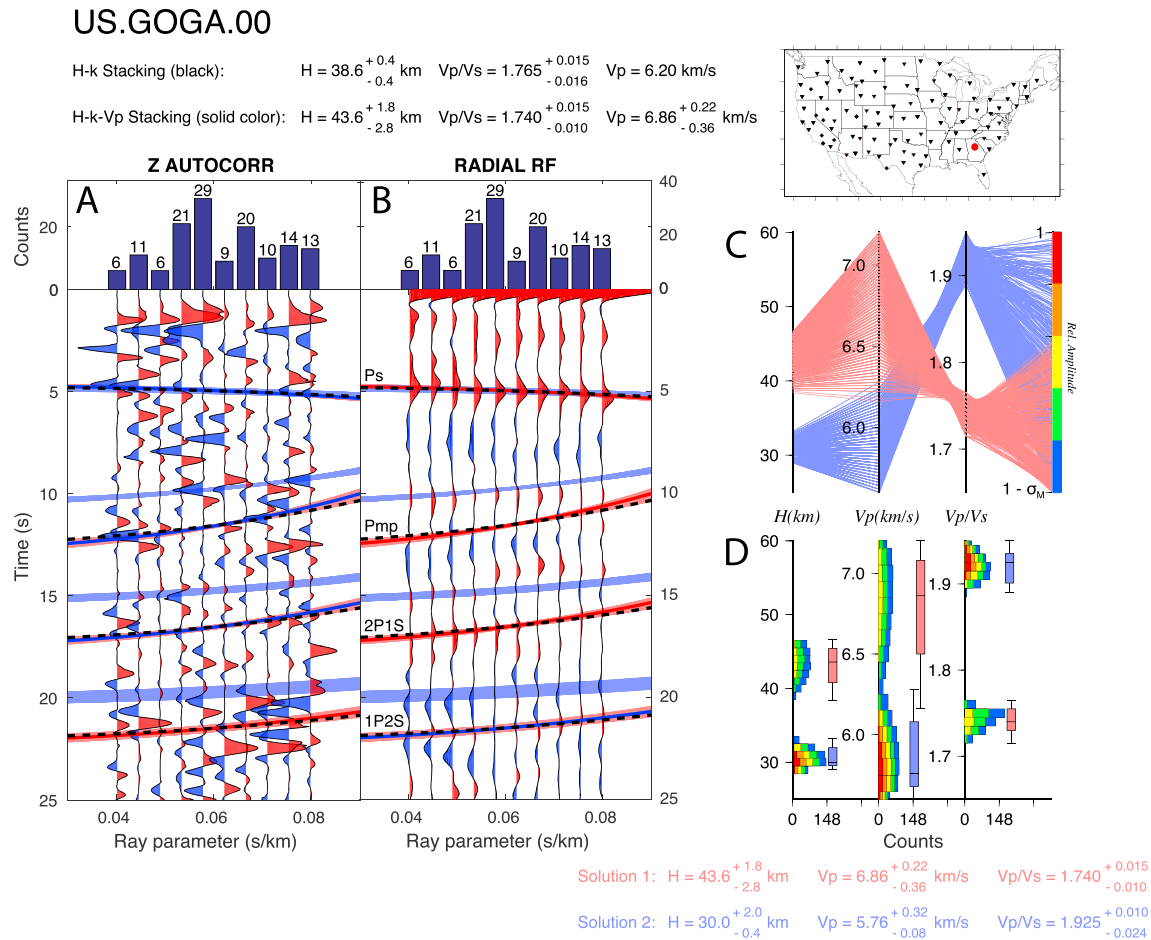


**Figure 10.** Analysis of station US.GOGA.00 located in Godfrey, Georgia (red dot on map). Results from  $H-\kappa$  and  $H-\kappa-V_p$  stacking analysis shown at the top. Predicted travel times for different phases calculated from the  $H-\kappa-V_p$  stacking analysis solution are colored by expected polarity of that phase (red = positive and blue = negative) on (a,b). Thin lines represent prediction from solutions within the standard error of the maximum stacking amplitude colored by cluster group. Black dashed lines represent solution from  $H-\kappa$  stacking analysis. (a) Vertical autocorrelations. (b) Radial receiver functions. (c) Parallel plot of  $H-\kappa-V_p$  solutions colored by group from cluster analysis. (d) Histogram of solutions colored by relative amplitude. Box and whisker plots show maximum amplitude (middle line) and middle 68.2% of the population distribution (box) along with the range of the “good” solutions (whiskers) and are colored by group from cluster analysis.

When compared to the average crustal  $V_S$  values of Schmandt et al. (2015), our results generally show a wider range of values for a given tectonic province (Figures 11e and 11f). We calculate  $V_S$  for our model by simply dividing our  $V_p$  solution by  $V_p/V_S$  ratio from  $H-\kappa-V_p$  stacking. To calculate the average crustal  $V_S$  from Schmandt et al. (2015), we take the average  $V_S$  above their crustal thickness estimates. The fundamental difference in the smoothness of the models likely stems from the smoothing associated with the inversion of interstation Rayleigh-wave phase velocities to 2-D maps, as opposed to our localized single station measurements. Anisotropy may also be playing a role in the disagreement of the  $V_S$  results, as Rayleigh waves are primarily sensitive to vertically-polarized shear wave velocities while receiver functions are more sensitive to horizontally-polarized shear wave velocities. Regardless, our  $V_S$  variations from  $H-\kappa-V_p$  stacking analysis appear more heterogeneous than one might expect and likely represent complexity related to local structure beneath stations that cannot be captured at the longer wavelengths of surface wave sampling. For example, in regions of complex crustal structure, multiply-reflected/converted phases from intracrustal discontinuities may interfere with signals generated from deeper primary structures, resulting in  $H-\kappa-V_p$  solutions that are erroneous. This heterogeneity is also reflected in the estimated  $V_p/V_S$  ratios (Figure 11g) similar to other continental-scale studies of these properties from  $H-\kappa$  analysis (e.g., EARS; Croftwell & Owens, 2005). Encouragingly, however, the slightly left-skewed distribution of  $V_p/V_S$  ratios is consistent

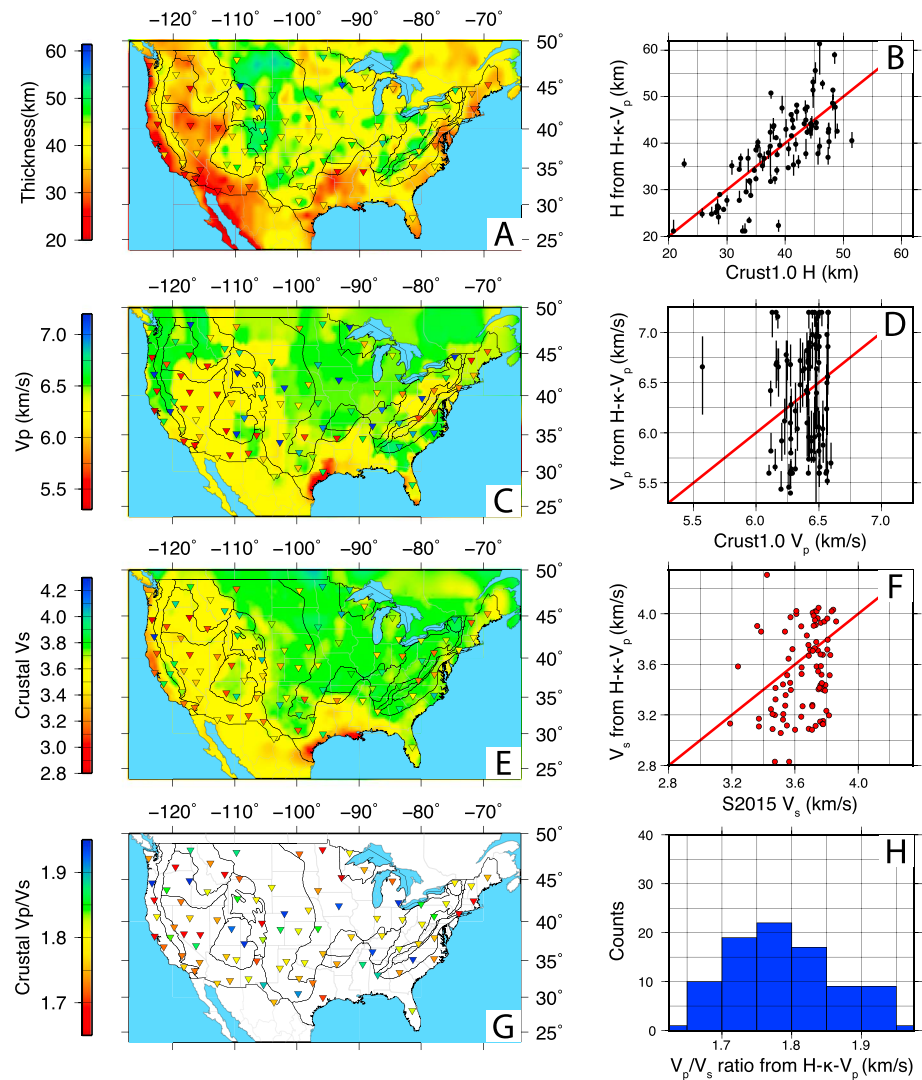


**Figure 11.** Comparison of crustal thickness (a,b),  $V_P$  (c,d), and  $V_S$  (e,f) estimates from different models and  $V_P/V_S$  ratio estimates from  $H\text{-}\kappa\text{-}V_P$  analysis (g,h). (a) Background surface colored by Crust1.0 results. Triangles: Stations colored by results of  $H\text{-}\kappa\text{-}V_P$  analysis. Black lines are different tectonic domains of the United States. (b) Comparison between our results (yaxis) at individual stations and Crust1.0 results (xaxis) at nearest grid point to our stations. Red line represents perfect agreement between measurements. (c) Background surface colored by Crust1.0  $V_P$  estimates, which are largely based on tectonic terrane. Triangles: Stations colored by results of  $H\text{-}\kappa\text{-}V_P$  analysis. (d) Same as (b) but for  $V_P$ . RMS difference: 0.59 km/s. (e) Background surface colored by Schmandt et al. (2015)  $V_S$  estimates. Triangles: Stations colored by results of  $H\text{-}\kappa\text{-}V_P$  analysis. RMS difference: 0.35 km/s. (g)  $V_P/V_S$  ratio results and solution distribution (h) from of  $H\text{-}\kappa\text{-}V_P$  analysis.

with the expected  $V_P/V_S$  ratio for a crust of silicic bulk composition ( $\sim 1.77$ ; Christensen & Mooney, 1995; Figure 11h).

## 5. Challenges Moving Forward

The  $H\text{-}\kappa\text{-}V_P$  stacking approach provides a new way to help constrain layer thickness and velocity properties using teleseismic data. The ability to add an independent observation to obtain the average  $P$ -wave velocity in a layer through the incorporation of coda autocorrelation provides a constraint on a parameter ( $V_P$ ) that is commonly assumed based on tectonic context or from sparsely deployed active source experiments (e.g., Christensen & Mooney, 1995; Laske et al., 2013). Perhaps, more importantly, however, this methodology

provides uncertainties for these measurements that can be used as a priori constraints for more detailed studies that use Bayesian methodologies, rather than simply assuming errors associated with the properties of interest. For instance, surface wave and receiver function joint inversions simply assume an initial  $V_S$  and crustal thickness using the results of other studies, holding  $V_P$  and commonly also  $V_P/V_S$  ratios constant (e.g., Delph et al., 2015; Shen et al., 2013). This can lead to uncertainties in crustal thicknesses that are underestimated by up to 20% (Shen et al., 2013). This will obviously also affect the accuracy of the a posteriori uncertainties of final shear velocities in these inversions, as it does not consider the contribution of variable  $V_P$  on surface wave phase velocities or the effects of  $V_P$  on the moveout of receiver function arrivals. By better constraining the average  $P$ -wave velocity structure, correlated uncertainties between  $V_P$ ,  $H$ , and  $V_P/V_S$  ratio can be more accurately quantified, propagated, and represented in detailed studies.

That the autocorrelation of body waves can provide an independent observation associated with the average  $P$ -wave velocity of a layer is certainly an improvement over a priori assumptions. However, the trade-off between  $V_P$  and  $H$  is still relatively low, and the recovered  $P_{mp}$  phase tends to be relatively low amplitude in practice. Possible ways to improve constraints on the recovered  $V_P$  could involve including  $S$ -wave receiver functions (e.g., Rychert & Harmon, 2016) and  $S$ -wave autocorrelations alongside the analysis presented here, as well as increasing the clarity of the phases in autocorrelations through improved processing techniques. Using the correlative methodologies of receiver functions and autocorrelations will allow for more representative and consistent models of crustal thickness and velocity structure as opposed to models created from methodologies with the inherently different sensitivities and resolutions (e.g., controlled-source data, receiver functions, and surface waves).

## 6. Conclusion

The  $P$ -wave coda of teleseismic earthquakes provides detailed information about the layered structure of the earth beneath a seismic station. Since Zhu and Kanamori (2000), body-wave conversions and their multiples have been analyzed via  $H$ - $\kappa$  stacking analysis of receiver functions to obtain the thickness ( $H$ ) and  $P$ - $S$  velocity ratio ( $\kappa$  or  $V_P/V_S$ ) in these layers. However, receiver functions have a weak sensitivity to  $P$ -wave velocity, leading most studies to hold this parameter fixed. This results in biased estimates of crustal properties as well as unquantified correlated uncertainties by not accounting for variability in  $P$ -wave velocity. As one use of receiver function results is to provide starting model constraints for more detailed seismic analyses, these underestimated uncertainties can propagate much further than the initial study. In this study, we apply a modified version of  $H$ - $\kappa$  stacking analysis ( $H$ - $\kappa$ - $V_P$  stacking) to 88 seismic stations that are spatially distributed throughout the United States. This analysis incorporates an amplitude term from the autocorrelation of the  $P$ -wave coda, which highlights Moho-reflected  $P$ -waves. As this waveform is independent of  $V_S$ , it provides an independent observation that can be leveraged to constrain the average  $P$ -wave velocity in a layer in the  $H$ - $\kappa$  stacking procedure. Uncertainties in  $P$ -wave velocity are also obtained through this approach, which allows for a more appropriate quantification of uncertainty in the final estimates by accounting for covariation between  $H$ ,  $V_P$ , and  $V_P/V_S$  ratio. Using this analysis, we present a coarse model of crustal properties throughout the United States that is unbiased by a priori assumptions and more accurately characterizes uncertainties in crustal properties.

## References

- Arthur, D., & Vassilvitskii, S. (2007). K-means++: The advantages of careful seeding. *in Proc ACM-SIAM symposium on discrete algorithms.*, doi: <https://doi.org/10.1145/1283383.1283494>.
- Christensen, N. I., & Mooney, W. D. (1995). Seismic velocity structure and composition of the continental crust: A global view. *Journal of Geophysical Research*, 100(B6), 9761–9788. <https://doi.org/10.1029/95JB00259>
- Claerbout, J. F. (1968). Synthesis of a layered medium from its acoustic transmission response. *Geophysics*, 33(2), 264–269. <https://doi.org/10.1190/1.1439927>
- Crotwell, H. P., & Owens, T. J. (2005). Automated receiver function processing. *Seismological Research Letters*, 76(6), 702–709. <https://doi.org/10.1785/gssrl.76.6.702>
- Delph, J. R., Levander, A., & Niu, F. (2018). Fluid controls on the heterogeneous seismic characteristics of the Cascadia Margin. *Geophysical Research Letters*, 45, 11,021–11,029. <https://doi.org/10.1029/2018GL079518>
- Delph, J. R., Zandt, G., & Beck, S. L. (2015). A new approach to obtaining a 3D shear wave velocity model of the crust and upper mantle: An application to eastern Turkey. *Tectonophysics*, 665, 92–100. <https://doi.org/10.1016/j.tecto.2015.09.031>
- Dempster, A. P., Laird, N. M., & Rubin, D. B. (1977). Maximum likelihood from incomplete data via the EM algorithm. *Journal of the Royal Statistical Society: Series B: Methodological*, 39(1), 1–22. <https://doi.org/10.1111/j.2517-6161.1977.tb01600.x>

## Acknowledgments

We thank two anonymous reviewers for their comments, which improved the manuscript. Codes to perform the autocorrelation and receiver function calculation and  $H$ - $\kappa$ - $V_P$  stacking are available on J. R. D.'s Github ([https://github.com/jrdelph/EQ\\_Autocorrelation](https://github.com/jrdelph/EQ_Autocorrelation)). J. R. D. was funded through the Wiess Post-doctoral Fellowship at Rice University. F. N. was funded through NSF Grant 1547228. The facilities of IRIS Data Services (<https://www.iris.edu>), and specifically the IRIS Data Management Center, were used for access to waveforms, related metadata, and/or derived products used in this study. IRIS Data Services are funded through the Seismological Facilities for the Advancement of Geoscience and EarthScope (SAGE) Proposal of the National Science Foundation under Cooperative Agreement EAR-1261681.

- Draganov, D., Campman, X., Thorbecke, J., Verdel, A., & Wapenaar, K. (2009). Reflection images from ambient seismic noise. *Geophysics*, 74(5), A63–A67. <https://doi.org/10.1190/1.3193529>
- Eagar, K. C., & Fouch, M. J. (2012). FuncLab: A MATLAB interactive toolbox for handling receiver function datasets. *Seismological Research Letters*, 83(3), 596–603. <https://doi.org/10.1785/gssrl.83.3.596>
- Eaton, D. W., Dineva, S., & Mereu, R. (2006). Crustal thickness and VP/Vs variations in the Grenville orogen (Ontario, Canada) from analysis of teleseismic receiver functions. *Tectonophysics*, 420(1-2), 223–238. <https://doi.org/10.1016/j.tecto.2006.01.023>
- Frasier, C. W. (1970). Discrete time solution of plane P-SV waves in a plane layered medium. *Geophysics*, 35(2), 197–219. <https://doi.org/10.1190/1.1440085>
- Frederiksen, A. W., & Bostock, M. G. (2000). Modelling teleseismic waves in dipping anisotropic structures. *Geophysical Journal International*, 141(2), 401–412. <https://doi.org/10.1046/j.1365-246X.2000.00090.x>
- Gorbatov, A., Saygin, E., & Kennett, B. L. N. (2013). Crustal properties from seismic station autocorrelograms. *Geophysical Journal International*, 192(2), 861–870. <https://doi.org/10.1093/gji/ggs064>
- Hawman, R. B., Khalifa, M. O., & Baker, M. S. (2012). Isostatic compensation for a portion of the Southern Appalachians: Evidence from a reconnaissance study using wide-angle, three-component seismic soundings. *Bulletin of the Geological Society of America*, 124(3-4), 291–317. <https://doi.org/10.1130/B30464.1>
- Heath, B. A., Hooft, E. E. E., & Toomey, D. R. (2018). Autocorrelation of the Seismic Wavefield at Newberry Volcano: Reflections From the Magmatic and Geothermal Systems. *Geophysical Research Letters*, 45, 2311–2318. <https://doi.org/10.1002/2017GL076706>
- Heinrich, J., & Weiskopf, D. (2013). State of the art of parallel coordinates: Eurographics 2013 - State of the Art Reports, p. 95–116.
- Inselberg, A. (2009). *Parallel coordinates: Visual multidimensional geometry and its applications*. New York, NY: Springer. <https://doi.org/10.1007/978-0-387-68628-8>
- Kennett, B. L. N. (2015). Lithosphere-asthenosphere P-wave reflectivity across Australia. *Earth and Planetary Science Letters*, 431, 225–235. <https://doi.org/10.1016/j.epsl.2015.09.039>
- Kennett, B. L. N., Saygin, E., & Salmon, M. (2015). Stacking autocorrelograms to map Moho depth with high spatial resolution in southeastern Australia. *Geophysical Research Letters*, 42, 7490–7497. <https://doi.org/10.1002/2015GL065345>
- Kim, D., Keranen, K. M., Abers, G. A., & Brown, L. D. (2019). Enhanced resolution of the subducting plate interface in Central Alaska from autocorrelation of local earthquake coda. *Journal of Geophysical Research: Solid Earth*, 124, 1583–1600. <https://doi.org/10.1029/2018JB016167>
- Langston, C. A. (1979). Structure under Mount Rainier, Washington, inferred from teleseismic body waves. *Journal of Geodynamics*, 84, 4749–4762.
- Laske, G., Masters, G., Ma, Z., Pasyanos, M.E., & Livermore, L., (2013). Update on CRUST1.0: A 1-degree global model of Earth's crust: *Geophys. Res. Abstracts*, 15,.
- Ligorria, J. P., & Ammon, C. J. (1999). Iterative deconvolution and receiver function estimation. *Bulletin of the Seismological Society of America*, 89, 1395–1400.
- Lin, F. C., Moschetti, M. P., & Ritzwoller, M. H. (2008). Surface wave tomography of the western United States from ambient seismic noise: Rayleigh and Love wave phase velocity maps. *Geophysical Journal International*, 173(1), 281–298. <https://doi.org/10.1111/j.1365-246X.2008.03720.x>
- Lin, F. C., Tsai, V. C., Schmandt, B., Duputel, Z., & Zhan, Z. (2013). Extracting seismic core phases with array interferometry. *Geophysical Research Letters*, 40, 1049–1053. <https://doi.org/10.1002/grl.50237>
- Lloyd, S. P. (1982). Least squares quantization in PCM. *IEEE Transactions on Information Theory*, 28(2), 129–137. <https://doi.org/10.1109/TIT.1982.1056489>
- McLachlan, G., & Peel, D. (2004). *Finite mixture models*, (p. 450). Hoboken, NJ: John Wiley & Sons.
- Niu, F., & James, D. E. (2002). Fine structure of the lowermost crust beneath the Kaapvaal craton and its implications for crustal formation and evolution. *Earth and Planetary Science Letters*, 200, 121–130. [https://doi.org/10.1016/S0012-821X\(02\)00584-8](https://doi.org/10.1016/S0012-821X(02)00584-8)
- Oren, C., & Nowack, R. L. (2017). Seismic body-wave interferometry using noise autocorrelations for crustal structure. *Geophysical Journal International*, 208(1), 321–332. <https://doi.org/10.1093/gji/ggw394>
- Phạm, T.-S., & Tkalčić, H. (2017). On the feasibility and use of teleseismic P wave coda autocorrelation for mapping shallow seismic discontinuities. *Journal of Geophysical Research: Solid Earth*, 122, 3776–3791. <https://doi.org/10.1002/2017JB013975>
- Phạm, T.-S., Tkalčić, H., Sambridge, M., & Kennett, B. L. N. (2018). Earth's correlation wavefield: Late coda correlation. *Geophysical Research Letters*, 45, 3035–3042. <https://doi.org/10.1002/2018GL077244>
- Poli, P., Campillo, M., & Pedersen, H. (2012). Body-wave imaging of Earth's mantle discontinuities from ambient seismic noise. *Science*, 338(6110), 1063–1065. <https://doi.org/10.1126/science.1228194>
- Poli, P., Pedersen, H. A., & Campillo, M. (2012). Emergence of body waves from cross-correlation of short period seismic noise. *Geophysical Journal International*, 188(2), 549–558. <https://doi.org/10.1111/j.1365-246X.2011.05271.x>
- Porritt, R. W., & Miller, M. S. (2018). Updates to FuncLab, a Matlab based GUI for handling receiver functions. *Computers and Geosciences*, 111, 260–271. <https://doi.org/10.1016/j.cageo.2017.11.022>
- Rychert, C. A., & Harmon, N. (2016). Stacked P-to-S and S-to-P receiver functions determination of crustal thickness, Vp, and Vs: The H-V stacking method. *Geophysical Research Letters*, 43, 1487–1494. <https://doi.org/10.1002/2015GL067010>
- Schimmel, M., & Paulssen, H. (1997). Noise reduction and detection of weak, coherent signals through phase weighted stacks. *Geophysical Journal International*, 130(2), 497–505. <https://doi.org/10.1111/j.1365-246X.1997.tb05664.x>
- Schmandt, B., Lin, F. C., & Karlstrom, K. E. (2015). Distinct crustal isostasy trends east and west of the Rocky Mountain Front. *Geophysical Research Letters*, 42, 10290–10298. <https://doi.org/10.1002/2015GL066593>
- Shapiro, N. M., Campillo, M., Stehly, L., & Ritzwoller, M. H. (2005). High-resolution surface-wave tomography from ambient seismic noise. *Science*, 307(5715), 1615–1618. <https://doi.org/10.1126/science.1108339>
- Shen, W., Ritzwoller, M. H., Schulte-Pelkum, V., & Lin, F.-C. (2013). Joint inversion of surface wave dispersion and receiver functions: A Bayesian Monte-Carlo approach. *Geophysical Journal International*, 192(2), 807–836. <https://doi.org/10.1093/gji/ggs050>
- Sun, W., & Kennett, B. L. N. (2017). Mid-lithosphere discontinuities beneath the western and central North China Craton. *Geophysical Research Letters*, 44, 1302–1310. <https://doi.org/10.1002/2016GL071840>
- Tibuleac, I. M., & von Seggern, D. (2012). Crust-mantle boundary reflectors in Nevada from ambient seismic noise autocorrelations. *Geophysical Journal International*, 189(1), 493–500. <https://doi.org/10.1111/j.1365-246X.2011.05336.x>

- Zandt, G., Myers, S. C., & Wallace, T. C. (1995). Crust and mantle structure across the Basin and Range-Colorado Plateau boundary at 37°N latitude and implications for Cenozoic extensional mechanism. *Journal of Geophysical Research*, *100*(B6), 10529–10548. <https://doi.org/10.1029/94JB03063>
- Zhu, L., & Kanamori, H. (2000). Moho depth variation in southern California from teleseismic receiver functions. *Journal of Geophysical Research*, *105*(B2), 2969–2980. <https://doi.org/10.1029/1999JB900322>